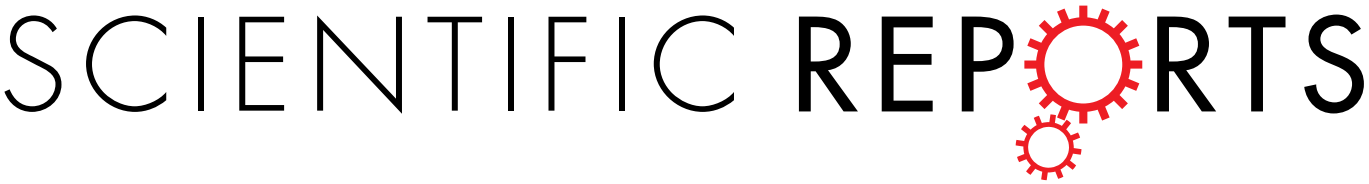

OPEN

Received: 15 February 2016
Accepted: 05 May 2016
Published: 03 June 2016

Terahertz radiation driven by two-color laser pulses at near-relativistic intensities: Competition between photoionization and wakefield effects

P. González de Alaiza Martínez*, X. Davoine*, A. Debayle*, L. Gremillet* & L. Bergé*

We numerically investigate terahertz (THz) pulse generation by linearly-polarized, two-color femtosecond laser pulses in highly-ionized argon. Major processes consist of tunneling photoionization and ponderomotive forces associated with transverse and longitudinal field excitations. By means of two-dimensional particle-in-cell (PIC) simulations, we reveal the importance of photocurrent mechanisms besides transverse and longitudinal plasma waves for laser intensities $>10^{15}$ W/cm^2. We demonstrate the following. (i) With two-color pulses, photoionization prevails in the generation of GV/m THz fields up to 10^{17} W/cm^2 laser intensities and suddenly loses efficiency near the relativistic threshold, as the outermost electron shell of ionized Ar atoms has been fully depleted. (ii) PIC results can be explained by a one-dimensional Maxwell-fluid model and its semi-analytical solutions, offering the first unified description of the main THz sources created in plasmas. (iii) The THz power emitted outside the plasma channel mostly originates from the transverse currents.

Terahertz (THz) radiation generated by ultrashort laser pulses has nowadays become an active topic of research due to many promising applications in security screening, cryptography, material sciences, medical imaging and remote detection of drugs and explosives[1–5]. Because these applications often request to probe unknown materials over long distances while overcoming absorption by atmospheric water molecules, there is a need for more and more intense THz signals with spectra tunable to the desired application. Several techniques exist to supply THz radiation, from conventional antennas to photoconductive switches, quantum cascade lasers, or by optical rectification in asymmetric crystals[6–10]. Most of them, based on solid emitters, appear to be limited by damage thresholds or by the narrowness of the emitted spectra. An alternative has been explored for more than ten years, consisting in mixing two different frequencies (colors) of intense femtosecond laser pulses inside a plasma spot that serves as a frequency down-converter in gases[11–13]. The resulting frequencies belong to the THz range. They can even be generated remotely in air through laser filaments[14–22], produced by the interplay between the Kerr response of bound electrons and first photoionization events taking place at intensities less than 10^{15} W/cm^2 in weakly ionized gases. Ultrabroad bandwidths up to 200 THz have also been measured in two-color gas plasma experiments[23], bridging quasi-continuously the THz and infrared regions of the electromagnetic spectrum.

Laser-driven THz generation is, however, not limited to nonlinear optics and is now emerging as a recurrent topic in relativistic laser-plasma interaction, for instance from solid targets irradiated at intensities $>10^{19}$ W/cm^2 [24–26]. In between these two working regimes lies a broad range of laser intensities, namely, $10^{15} \leq I_L < 10^{18}$ W/cm^2, for which a plasma formed by laser-gas interaction usually involves high ionization levels and plasma waves produced in the wake of the laser field. So far, a number of papers have addressed THz wave generation by single-color pulses in classical plasma regimes[27–30]; some of them even examined the influence of external magnetic fields resulting in higher conversion efficiencies through three-wave parametric decay[31]. Much fewer have been devoted to two-color pulses[32–35]. With two colors, a well-known scenario for THz pulse generation is the photocurrent mechanism, following which ionization events in the tunneling regime accumulated along asymmetric pulse

CEA-DAM, DIF, F-91297 Arpajon, France. *These authors contributed equally to this work. Correspondence and requests for materials should be addressed to P.G.d.A.M. (email: pedro.gonzalesdealaiza@cea.fr)

profiles produce a low-frequency current responsible for THz wave emission[36]. The robustness of this so-called photocurrent scenario at intensities above 10^{15} W/cm^2 is, nonetheless, an open issue. Indeed, alternative key players may be longitudinal and transverse plasma waves promoted by the laser-induced ponderomotive forces[28,37] or ionization-induced plasma current oscillations[38,39]. A pure one-dimensional (1D) configuration without ponderomotive effects was investigated by some of the present authors[35], but a multidimensional analysis is necessary to discriminate between all the different THz sources.

In this paper, two-dimensional (2D) particle-in-cell (PIC) simulations display evidence that the photocurrent mechanism is mostly responsible for THz pulse generation at laser intensities above 10^{16} W/cm^2 and produces GV/m field strengths in argon. However, when the relativistic intensity threshold is approached ($I_L \to 10^{18}$ W/cm^2), single-color and two-color pulse schemes offer similar field strengths. Close to the relativistic limit, the conversion efficiency saturates in Ar because the charge number $Z^* = 8$ corresponds to a stable electronic configuration[35] that turns off the photocurrent mechanism. By increasing the laser intensity from 10^{15} to 3×10^{17} W/cm^2, we reveal the enhanced action of longitudinal plasma waves inside the plasma channel, as the ion charge number is increased in the interval $2 \le Z^* \le 8$. There, photoionization and longitudinal ponderomotive force act as the most efficient THz converters, whose characteristic properties are supported by a one-dimensional (1D) model unifying the THz source terms. Nevertheless, the longitudinal electrostatic fields created inside the plasma barely contribute to the outward emission of the electromagnetic fields. The transverse ponderomotive effects, instead, sustain the THz field radiated away from the plasma. As a matter of fact, we show that the magnetic field component parallel to the laser polarization axis does provide a reliable measurement of THz emissions by plasma ponderomotive forces, while the electric field polarized in the same direction mostly arises from photocurrent sources.

Results

2D particle-in-cell simulations. For a few years there has been a wide consensus on the directivity of the energy radiated by a laser-created plasma spot[22,33,34,40,41]. THz emission by a plasma is usually evaluated through the flux of Poynting vector $\vec{S} = (c/\mu_0)|\vec{\nabla} \times \vec{A}|^2 \vec{n}$, where $\vec{A}$ and $\vec{n}$ are the vector potential and propagation unit vector of the THz radiated field, respectively (c and μ_0 are the speed of light and magnetic permeability in vacuum). Denoting by $\vec{J}$ the current associated with this vector potential, $\vec{A}(\vec{r}, t) = (\mu_0/4\pi) \int \vec{J}(\vec{r'}, t')\,|\vec{r} - \vec{r'}|^{-1} d\vec{r'}$ where $t' = t - |\vec{r} - \vec{r'}|/c$, the energy spectral density of the electromagnetic radiation per unit of solid angle Ω is computed in the far-field approximation ($r \gg r'$, c/ω) as[37]

$$\frac{d^2\mathcal{E}}{d\omega d\Omega} = \frac{cr^2}{\pi\mu_0}|\vec{\nabla} \times \widehat{\vec{A}}(\omega, \vec{r})|^2 = \frac{\omega^2 L^2}{16\varepsilon_0 \pi^3 c^3} \mathrm{sinc}^2\left[\frac{\omega L}{c}(1 - \cos\theta)\right] |\vec{n} \times \widehat{\vec{J}}(\omega, \vec{k}_\perp)|^2. \quad (1)$$

Here, $\widehat{\vec{J}}(\omega, \vec{k}_\perp)$ is the Fourier transform of the radiating current density expressed in the pulse retarded time $\tau \equiv t - z/c$ and in the (x, y) plane, ω is the pulse frequency, $\vec{k}_\perp$ denotes its transverse wavevector, ϕ is the azimuthal angle while θ is the polar angle between $\vec{n}$ and the laser field wavevector along the propagation axis [$k_z = (\omega/c)\cos\theta$]. Equation (1) holds for a current density $\vec{J}$ assumed to be uniform over the propagation axis z and whenever the laser pulse components (colors) have walk-off and phase mismatch lengths much longer than the plasma length L. In the following, modulations induced by mismatching between laser harmonics due to optical path difference are avoided by working with short enough plasma length ($L \approx 100\,\mu$m). From Eq. (1) the directivity of a plasma-induced THz emission is linked to that of the current density $\vec{J}$ triggered by different source terms, such as photoionization or ponderomotive forces. This link is expected to provide crucial information on the nonlinearities prevailing in the far-field THz emissions, since the factor $|\vec{n} \times \widehat{\vec{J}}|^2 = \sum_j |\hat{J}_j|^2 f_j(\theta, \phi)$ with $j = x, y, z$ has characteristic angular distributions $f_j(\theta, \phi) = 1 - (\vec{n} \cdot \vec{e}_j)^2$, where $\vec{n} = \sin\theta\cos\phi\,\vec{e}_x + \sin\theta\sin\phi\,\vec{e}_y + \cos\theta\,\vec{e}_z$. In particular, if longitudinal forces are dominant ($f_z = \sin^2\theta$), the angular distribution of the radiated power flow exhibits multiple (N) lobes at angular positions fixed by the relationship $\theta = 2\sin^{-1}(\sqrt{N\lambda/4L})$, $\lambda = 2\pi c/\omega$ being the emission wavelength. The angular pattern here consists of two off-axis symmetric lobes ($N = 1$) and the opening angle is inversely proportional to the plasma length. When transverse forces instead prevail, the geometrical factors f_x, f_y are close to unity for small angles $\theta \ll 1$ and the central lobe is filled, up to small conical deviations $\ll 10°$ [21]. This feature holds except if $\widehat{J_y}$ vanishes on-axis ($k_\perp = 0$), which will be the case for a ponderomotively driven current.

Let us recall that the applicability of equation (1) is, nevertheless, limited. Indeed, this relationship is based on a wire-antenna model that implicitly assumes no transverse variations of charge distributions. Radial ponderomotive forces do not affect the plasma channel when its transverse radius r_p is much smaller than the emission wavelength $\lambda \approx c/\omega_{pe}$ and when THz emission proceeds from electron plasma waves with frequency ω_{pe}. The opposite inequality, $r_p \gg c/\omega_{pe}$, can also be applied to ignore transverse gradients of the laser envelope[28]. In this configuration, there is a radial component of plasma current density that induces a surface charge at the plasma-gas boundary. For a steady-state plasma, the axial (longitudinal) mode associated with J_z rapidly vanishes as $r_\perp^{-1/2}\exp(-\kappa_\perp r_\perp)$ outside the plasma zone together with the radial component ($r_\perp = \sqrt{x^2 + y^2}$, $\kappa_\perp$ is a real eigenvalue). The relevant field component is the azimuthal magnetic field B_θ decreasing more slowly as $\sim r_\perp^{-2}$ over large distances. For a non-steady plasma undergoing longitudinal ponderomotive modulations with wavenumber κ_z, transverse modes with pure imaginary $\kappa_\perp$ can be triggered and they form efficient radially outgoing waves emitted along the Cerenkov angle $\theta_c = \tan^{-1}(|\kappa_\perp|/\kappa_z)$ with superluminal phase velocity. Little information is, however, available on plasma geometries with finite transverse extents, for which the previous literature suggests

that only the plasma-gas boundaries should emit within the plasma skin depth. To our knowledge, THz emission by photocurrents has moreover never been addressed in this context.

Below we clear up this issue and identify the main sources of THz emission at high laser intensities $\geq 10^{15}$ W/cm^2. We performed PIC simulations using the two-dimensional version of the CALDER code (see Methods)[42]. A laser pulse polarized along the x-axis is propagated along a 100-μm-long plasma of a 2D-geometrical (y, z) argon gas. The initial density profile is trapezoidal, with a 90-μm-long plateau bordered by 5-μm-long linear ramp at each side. The initial ion temperature is 1 eV and the initial neutral density, $N_a = 2.4 \times 10^{17}$ cm^{-3}, guarantees an underdense plasma even at the highest intensities considered. We simulate a Gaussian pulse both in space and time in the form

$$E_L(t, y, 0) = \sqrt{\frac{2I_0}{c\varepsilon_0}}\, e^{-\left(\frac{y}{w_0}\right)^2}\left[\sqrt{1-r}\, e^{-2\ln 2\left(\frac{t}{\tau_p}\right)^2}\cos(\omega_0 t) + \sqrt{r}\, e^{-8\ln 2\left(\frac{t}{\tau_p}\right)^2}\cos(2\omega_0 t + \varphi)\right], \quad (2)$$

where I_0 is the mean pump intensity, r is the relative intensity ratio of the second harmonic and $\varepsilon_0 = 1/\mu_0 c^2$. The relative phase φ between the fundamental with carrier frequency ω_0 and second harmonic is initially set to $\pi/2$. This phase offset optimizes local photocurrents[12,36,43]; however, as the relative phase evolves along propagation, the gain factor achieved with another initial phase offset would remain of similar order of magnitude (see Supplementary Information). The FWHM duration of the pump pulse centered at 1-μm wavelength is $\tau_p = 35$ fs and its $1/e^2$ transverse width along y is $w_0 = 20\,\mu$m, allowing to form a rather thick plasma. We always consider an intensity ratio r of 0.1 between the fundamental pump and its second harmonic (0.5-μm wavelength) when two colors are employed ($r = 0$ for a single color). Our intensity range, $I_0 \leq 3 \times 10^{17}$ W/cm^2, corresponds to the normalized laser vector potential $|a_L| = e|A_L|/m_e c^2 \leq 0.5$, where e and m_e are the electron charge and mass. The maximum values of ω_{pe}, which initiate the THz spectra, are then comprised between $0.02\omega_0$ and $0.04\omega_0$ in argon, i.e., $\nu_{pe} \equiv \omega_{pe}/2\pi = 6$–$12$ THz. The CALDER code encompasses all necessary plasma physics, from multiple photoionization in the tunnel regime to kinetic, collective and plasma wakefield effects, in and beyond classical plasma regimes adapted to, e.g., the physics for laser-plasma accelerators. The different radiated field components ($\widetilde{E}_x$, $\widetilde{E}_y$, $\widetilde{E}_z$) and their magnetic counterparts ($\widetilde{B}_x$, $\widetilde{B}_y$, $\widetilde{B}_z$), indicated with tilde symbol, are extracted from the PIC simulations. Forward radiation is only regarded in the present study and the transverse field E_x includes both the laser field E_L and the secondary (radiated) field $\widetilde{E}_x$. Secondary fields are polarized along their respective current densities J_x, J_y and J_z, which, by virtue of Eq. (1), should contain the spectral signature of the THz source terms at remote distances from the plasma channel. In our 2D (y, z) geometry, the relationship $\vec{J} = -\varepsilon_0 \partial_t \vec{E} + \mu_0^{-1} \vec{\nabla} \times \vec{B}$ invites us to map the THz spectrum yielded by J_x from E_x in order to capture photocurrents only, and use $B_x = \partial_y E_z - \partial_z E_y$ to isolate contributions subject to the ponderomotive forces acting in the orthogonal plane.

Although our simulation parameters are chosen for an academic purpose, they can be approached using gas-jet tailoring techniques developed for laser-wakefield accelerators. In this setting sharp downward density transitions are created through shock fronts induced either by a knife edge or by nanosecond laser pulses into a supersonic gas target[44,45]. A typical scheme could here employ 35-fs, 70-mJ pump pulses focused into a vacuum chamber by a $f/10$ off-axis mirror (numerical aperture ~0.02) and passing through a 0.1 mm thin β-barium borate (BBO) crystal. At the centre of the vacuum chamber, the nozzle delivering a supersonic Ar-gas jet would host a razor blade mounted laterally, allowing to switch a shock front transversally along the laser propagation axis and to monitor density gradients over ~10 μm lengths. The forwardly emitted THz radiation would then be collected by a parabolic mirror and directed toward a pyroelectric detector equipped with a silicon filter.

Figure 1 shows our principal result which, to the best of our knowledge, consists of the first spectral mapping of laser-plasma-based THz generation accounting for both photocurrents and ponderomotive forces in multidimensional geometry. From top to bottom are presented the spectra of the radiated field component $\widetilde{E}_x$ and of the transverse magnetic field $\widetilde{B}_x$. The two-color laser field is linearly polarized on the x-axis, along which no propagation or plasma interaction effects occur. The angular distribution in (k_y, k_z) of $\widetilde{E}_x$ thus reflects in Fourier space THz emission by photoionization, since $\partial_t \widetilde{E}_x \sim J_x \sim \omega_{pe}^2 E_L$ (see equation for $\vec{J}$ above). Here the electron plasma frequency $\omega_{pe} = \sqrt{e^2 N_e/\varepsilon_0 m_e}$ increases with the free electron density $N_e(t)$ along fast ionization steps[36] and reaches its maximum value beyond the laser region. Along the same direction, the polar emission map of $\widetilde{B}_x$ displays THz radiation from $\widetilde{E}_y$, $\widetilde{E}_z$, which excludes photoionization but keeps the trace of ponderomotive effects in the $y-z$ plane.

For the main three intensity levels investigated here, (10^{15}, 5×10^{16} and 3×10^{17} W/cm^2), THz emissions forwarded beyond the plasma zone ($z = 175\,\mu$m) exhibit similar spectral signatures. Photocurrents induced by tunneling ionization are known to play a major role in THz generation from gases irradiated by two-color laser pulses at filamentation intensities ~10^{14} W/cm^2 [19]. Recently, this property was confirmed by direct measurements supported by numerical simulations of two-color filaments in air, the plasma response of which was shown to take over the Kerr nonlinearity in the conversion process, shifting the peak of the THz spectrum towards the electron plasma frequency[46]. For one order of magnitude larger intensities, photocurrents again persist as being the major mechanism in driving THz emissions, whereas single-color pulses mostly initiate THz radiation from plasma wakefields [compare Fig. 1(a) and Fig. 1(b)]. One or two-color schemes do not change the ponderomotive contributions to the THz yield. The E_x-field spectra, peaked on-axis ($\theta = 0$), decay at larger θ angles according to the sinc function of Eq. (1). At laser intensities high enough to promote large ion charge numbers $Z^* = N_e/N_a \to 8$, photoionization still competes with ponderomotive effects for emitting THz electromagnetic fields, despite the important strength of the ponderomotive sources [see Fig. 1(c)]. Close to the relativistic limit, $I_0 = 3 \times 10^{17}$ W/cm^2, the conversion efficiency due to photocurrents somewhat saturates, but goes on delivering intense THz

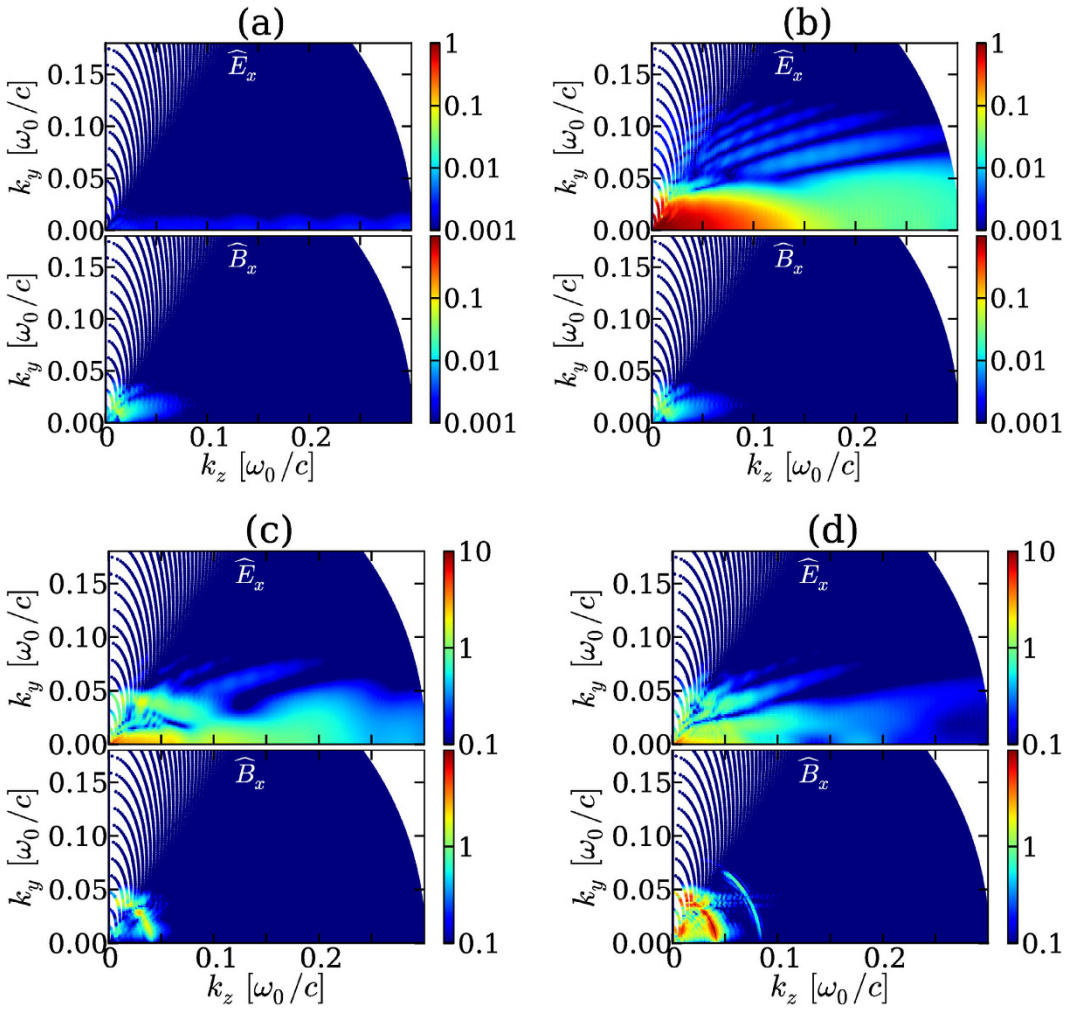

Figure 1. Spectral angular distribution of THz radiation (arb. units) in the (k_y, k_z) plane produced by E_x and B_x along the laser polarization axis in the following configurations: (**a**) Single-color pulse and (**b**) two-color pulse with mean intensity I_0 of 10^{15} W/cm^2; (**c**) two-color pulse with 5×10^{16} W/cm^2 and (**d**) two-color pulse with 3×10^{17} W/cm^2. The fields are recorded as a function of t and y at the given position $z = 175\,\mu$m (outside the plasma zone) and their spectra are discretized on a uniform, Cartesian mesh as a function of ω and k_y. Due to the quadratic dependence of $k_z^2 = \omega^2/c^2 - k_y^2$ on ω and k_y, the fields are plotted on a non-uniform mesh as a function of k_z and k_y. Each point in the (k_z, k_y) space is represented by a color dot. The overlap of the dots creates the color map; this overlap cannot be achieved for the very low frequencies $k_z \ll k_y$.

pulses [Fig. 1(d)]. In summary, along x, photocurrents increase the THz yield as the pump intensity is augmented till saturation at near-relativistic intensity. THz components due to ponderomotive emitters along the orthogonal directions, by contrast, monotonically increase.

A simplified model for *in-situ* THz emitters. Understanding the previous results requires to scan the field dynamics initiated inside the plasma channel. For simplicity, we use a reduced model discriminating THz emitters only promoted by the x– and z–polarized fields, since photocurrents generate THz pulses along the laser polarization axis and propagation aspects mainly concern the longitudinal axis. Discarding ion motions, the current density induced by the photoionized electrons is $\vec{J} \simeq -eN_e\vec{v}_e$, where N_e and $\vec{v}_e$ are the free electron density and velocity. The electron current obeys the following equation set[28]

$$(\partial_t + \nu_c)\gamma\vec{J} = \frac{e^2}{m_e}N_e\vec{E} + \vec{\Pi}, \tag{3}$$

$$\vec{\Pi} = -\frac{e}{m_e}\vec{J} \times \vec{B} + (\vec{J}\cdot\vec{\nabla})\left(\frac{\gamma\vec{J}}{eN_e}\right) + \frac{\gamma\vec{J}}{N_e}(\partial_t N_e - S_{\text{ext}}), \tag{4}$$

where $\gamma = (1 - v_e^2/c^2)^{-1/2}$ is the relativistic factor, ν_c is the electron collision rate, $\overrightarrow{B}$ is the magnetic field associated with the total electric field $\overrightarrow{E}$ that includes both the laser field and secondary (THz) radiation. The last term of Eq. (4) originates from external drivers, such as photoionization, electron recombination or attachement. Over femtosecond time scales, only photoionization plays a role. This process is described using an Ammosov-Delone-Krainov (ADK)-based multiple ionization scheme[47] that involves the increase in ion densities gathered within the source term $S_{\text{ext}} = \sum_j j\partial_t N_j$ (see Methods). In our selected intensity range, tunnel ionization indeed prevails as argon atoms are never fully ionized and their electron shells undergo multiple sequential ionization. The other terms refer to the radiation pressure and ponderomotive forces, which may be evaluated using envelope substitutions, i.e.,

$$\overrightarrow{E}_L = \frac{1}{2}(\mathcal{E}_{\omega_0} e^{i\psi_{\omega_0}} + \mathcal{E}_{2\omega_0} e^{i\psi_{2\omega_0}} + c.c.)\overrightarrow{e}_x,\ \psi_{\Omega_0} = k(\Omega_0)z - \Omega_0 t,\ \Omega_0 = \omega_0, 2\omega_0, \tag{5}$$

where $|\partial_t \mathcal{E}_{\Omega_0}| \ll \Omega_0 |\mathcal{E}_{\Omega_0}|$. Combining Eqs (3) and (4) with Maxwell equations provides the propagation equation for the overall electric field $\overrightarrow{E}$ and yields the full three-dimensional Maxwell-fluid model. This is reduced to a one-dimensional (z-propagating) model by discarding the diffraction operators ($\partial_x = \partial_y = 0$) in the transverse plane together with chromatic dispersion. Since our intensity range remains sub-relativistic, we moreover omit variations of the relativistic factor and $\gamma \simeq (1 + a_L^2)^{1/2}$ is viewed as a constant. In this regime the nonlinear source term $\overrightarrow{\Pi}$ is evaluated on the laser field propagating forward with the sole variable $(z - ct)$. Ignoring terms in $(\overrightarrow{J} \cdot \overrightarrow{\nabla})\overrightarrow{J}$ at leading order and assuming $B_y = -\partial_z \int_{-\infty}^{t} E_x dt' = E_x/c$ for B_y travelling like the laser pulse, our model equations for the transverse and axial fields are:

$$(\partial_t^2 - c^2\partial_z^2 + \partial_t(\partial_t + \nu_c)^{-1}\tilde{\omega}_{\text{pe}}^2)\tilde{E}_x = -\frac{1}{\varepsilon_0}\partial_t J_L, \tag{6}$$

$$(\partial_t^2 + \nu_c\partial_t + \tilde{\omega}_{\text{pe}}^2)\tilde{E}_z = \frac{e}{m_e\varepsilon_0\gamma c} J_L E_L. \tag{7}$$

They both involve the current density computed on the laser field, $J_L = \varepsilon_0(\partial_t + \nu_c)^{-1}\tilde{\omega}_{\text{pe}}^2 E_L$, and the modified electron plasma frequency

$$\tilde{\omega}_{\text{pe}}^2 \equiv \frac{e^2}{\gamma\varepsilon_0 m_e}\sum_{j=0}^{Z} jN_j, \tag{8}$$

that incorporates the fast growth of ion densities N_j over attosecond ionization time scales. At high intensities, temporal modulations of $N_e(t)$ due to plasma wakefield is described by the relationship $N_e(t) = -J_z(t)/ec + \sum_{j=0}^{Z} jN_j(t)$.

The transverse field contains two contributions to THz emission: (i) the coupling between $N_e(t) \sim \sum_j jN_j(t)$ and the high-frequency field $E_L(t)$ creating photocurrents through the laser current density $J_L\overrightarrow{e}_x$ and (ii) plasma current oscillations developing over long times[36,39]. With two colors, the product between the fast variations of $N_e(t)$ and those of $E_L(t)$ acts as an efficient converter to low frequencies and promotes slow current components associated with THz generation in the beam head[13]. By comparison, the longitudinal field equation (7) describes THz emission from plasma oscillations that develop over picosecond time scales after the laser field has interacted with the gas. Collisions are weak ($8.83 \times 10^{-5} \le \nu_c \le 5 \times 10^{-3}\,\text{fs}^{-1}$, see Methods) and THz emissions due to longitudinal fields are mainly triggered by ponderomotive excitations[28,37].

Figure 2(a–f) proceed with a direct comparison between the on-axis transverse (x) and axial (z) components of the electromagnetic field emitted in a 90-THz wide frequency window ($\omega/\omega_0 < 0.3$) at the middle of the plasma channel, $z = 50\,\mu$m. Black, blue and green curves in solid lines refer to CALDER computations for increasing intensities; dashed curves plot the corresponding solutions to Eqs (6) and (7) with the same color plotstyle. The latter equation for $\tilde{E}_z$ is solved as an ordinary differential equation by a classical Runge-Kutta method; the former for $\tilde{E}_x$ is a linear transport equation solved through standard upwind finite difference schemes. Equation (6) indicates that the transverse radiated field strength intrinsically depends on the longitudinal gradients. Compared with antecedent studies assuming *a priori* $\tilde{E}_x \propto \partial_t J_L$[36], Eq. (6) directly provides the correct field strength with no need of geometrical factor[48]. The dominant part of its solution is a single-cycle pulse due to photoionization, as plasma current oscillations only form a residual tail modulated at plasma frequency [Fig. 2(a–c)]. The axial field is connected with plasma wave oscillations, where the plasma frequency increases like $\sqrt{N_e}$, i.e., with the ionization state Z^* when the laser intensity is increased [Fig. 2(d–f)]. For each intensity value, Fig. 2 displays evidence of a very good agreement between 2D PIC computations and our 1D model. Small discrepancies occur in the THz pulse profiles at near-relativistic intensity. These are linked to two-dimensional effects (e.g., transverse diffraction), small deviations from the assumption of constant γ, and the non-negligible influence of electron-electron collisions. They, however, preserve an accurate estimate of the THz field strength. Our 1D model provides us with an analytical evaluation for the transverse emitted field (see Methods):

$$\tilde{E}_x(z, t) \approx -\frac{z}{2c}\int_{-\infty}^{t-z/c} e^{-\nu_c(t-t')}\tilde{\omega}_{\text{pe}}^2(t')E_L(t')dt', \tag{9}$$

while the axial field recovers the standard form ($\nu_c \ll \tilde{\omega}_{\text{pe}}$)

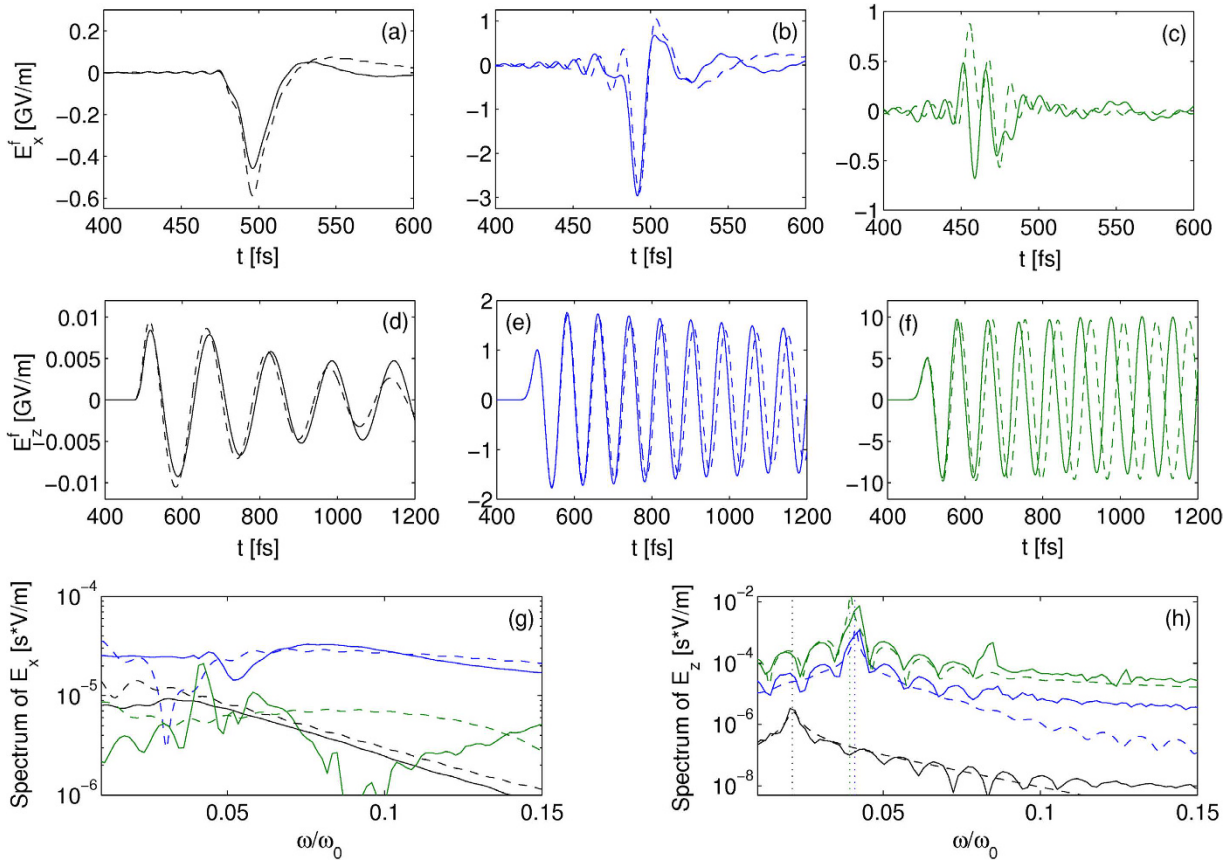

Figure 2. Comparison between 2D PIC results (solid curves) and semi-analytical solutions of the 1D model (dashed curves) for the on-axis electric fields (top row) $\widetilde{E}_x$ and (middle row) $\widetilde{E}_z$ emitted by two-color pulses inside the plasma channel at $z = 50\,\mu$m for the mean pump intensity (**a,d**) $I_0 = 10^{15}$ W/cm^2 (black curves), (**b,e**) $I_0 = 5 \times 10^{16}$ W/cm^2 (blue curves), and (**c,f**) $I_0 = 3 \times 10^{17}$ W/cm^2 (green curves). (Bottom row) On-axis spectra of the radiated fields (**g**) $\widetilde{E}_x$ and (**h**) $\widetilde{E}_z$ with same color plotstyles. The vertical dotted lines indicate values of the plasma frequency.

$$\widetilde{E}_z(t) \approx \frac{e}{4\gamma m_e c}\int_{-\infty}^{t} \widetilde{\omega}_{\mathrm{pe}}(t')\,\mathrm{e}^{-\nu_c(t-t')/2}\,\sin\left[\int_{t'}^{t}\widetilde{\omega}_{\mathrm{pe}}(t')\,dt'\right]\partial_{t'}\sum_{\Omega_0}\frac{\left|\mathcal{E}_{\Omega_0}(t')\right|^2}{\Omega_0^2}dt'. \tag{10}$$

Maximum achievable field strengths are 3 GV/m for the transverse field produced at 5×10^{16} W/cm^2 and 10 GV/m for the longitudinal field emitted at 3×10^{17} W/cm^2 inside the plasma. These are record values reported in this context.

Figure 2(g,h) detail the spectral dynamics inferred from our 1D model for increasing intensities. Again we let the pulse propagate over 100 μm of plasma, then filter out the emitted fields at $z = 50\,\mu$m. The dotted vertical lines locate the plasma frequency $\widetilde{\omega}_{\mathrm{pe}}$ achieved in the wake of the laser field and expressed in ω_0 units. In Fig. 2(h) the spectrum of the longitudinal field remains highly peaked around the plasma frequency, as justified by its direct dependency on $I_0(\omega^2 + i\nu_c\omega - \widetilde{\omega}_{\mathrm{pe}}^2)^{-1}$, which can easily be sorted out from Eq. (7). By contrast, the spectrum of the transverse field increases in amplitude and toward "long" wavelengths with the laser intensity, before saturating at 3×10^{17} W/cm^2 [Fig. 2(g)]. Its analytical expression established by taking the Fourier transform of Eq. (6) reads as

$$\widehat{\widetilde{E}}_x(z,\omega) = g(z,\omega)\widehat{\partial_t J_L(t)}, \tag{11}$$

assuming a constant plasma frequency, where the z-dependent function $g(z,\omega)$ can be found detailed in the Methods section. With a constant g one retrieves the well-know local current relationship $\widehat{\widetilde{E}}_x \propto \widehat{\partial_t J_L(t)}$[36]. Initiated around the plasma frequency ($0.02 < \omega_{\mathrm{pe}}/\omega_0 \leq 0.04$), the transverse THz spectrum develops a broad extent comparable with the patterns of Fig. 1. The overall agreement between PIC simulations and our 1D solutions is good, except in the very low-frequency limit.

Figure 3(a) confirms that, at the highest intensity $I_0 = 3 \times 10^{17}$ W/cm^2, the y-polarized fields induced by transverse ponderomotive forces generate *in-situ* off-axis THz components ($\Pi_y \propto \partial_y E_L^2$) being weaker than their longitudinal counterpart [compare with Fig. 2(f)]. This justifies a posteriori our 1D model. At the same intensity level

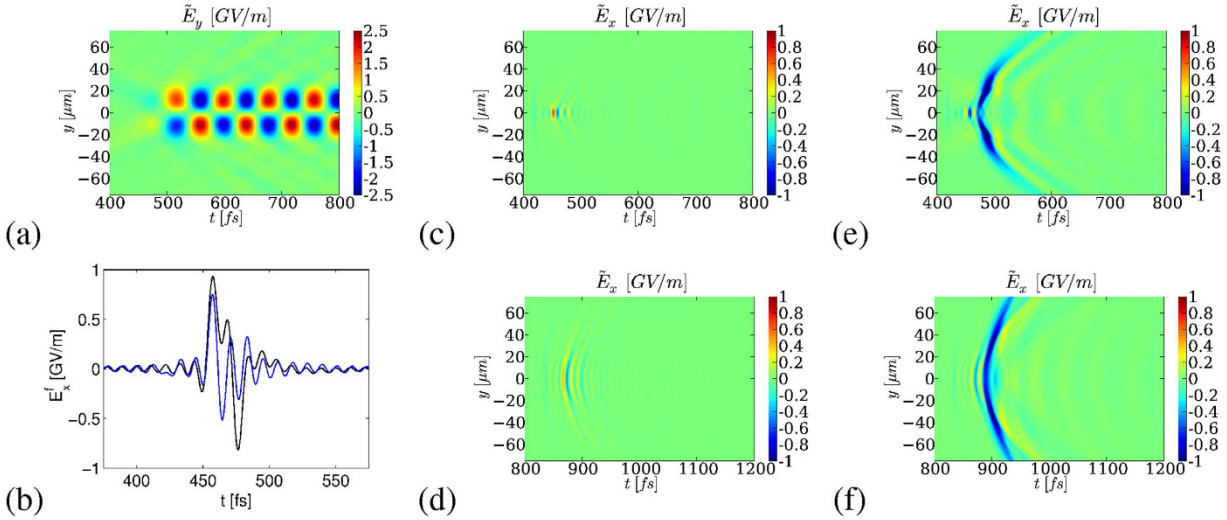

Figure 3. (**a**) 2D PIC spatio-temporal map of $\widetilde{E}_y$ triggered by two-color pulses for $I_0 = 3 \times 10^{17}$ W/cm^2. (**b**) 2D PIC simulation (blue curve) and 1D semi-analytical solution (black curve) of the on-axis x-polarized radiated field at $z = 50\,\mu$m for a single color with the same intensity. Spatio-temporal maps $\widetilde{E}_x(y,\ t)$ for (**c**) a single-color pulse and (**e**) a two-color pulse at the same distance and intensity. (**d,f**) Same patterns at remote distance $z = 175\,\mu$m outside the plasma channel. The color bars of (**c–f**) are cut at ± 1 GV/m for better visibility of the emitted waves. Note the change of scale in time.

and for one color, the on-axis CALDER field $\widetilde{E}_x$ and its semi-analytical evaluation are shown in Fig. 3(b), evidencing that our semi-analytical model again provides reliable approximations at near-relativistic intensities for a single-color pulse, apart from the aforementioned discrepancies. By comparison of this subplot with Fig. 2(c), we can observe that both the single- and two-color pulse schemes supply analogous on-axis x-field strengths (~GV/m). The maximum THz field amplitudes delivered by tunnel ionization being located on-axis, one infers a clear saturation in the conversion efficiency of the two-color scheme near the relativistic intensity threshold. The reason of this saturation is that, at intensities close to 10^{18} W/cm^2, Ar atoms have their outermost electron shell empty ($Z^* = 8$); so the remaining ion is shaped into a stable Ne-like atom configuration. This property manifests itself by a long plateau in the curve Z^* versus I_0[35], signaling the hardness to further ionize the ion. Approaching $Z^* = 9$ with 1.4×10^{18} W/cm^2 intensities re-activates the two-color pulse efficiency by the delivery of 7.6 GV/m THz transverse fields (not shown), which, however, remains comparable with the present performances. This explains why the ionization process loses efficiency near relativistic intensities. The same saturation phenomenon can be expected in other gases, for instance helium, once the available two electrons have been ionized at similar intensities. It is worth noticing that although photocurrents cannot produce stronger THz fields, they can supply more energetic THz pulses as the volume of the secondary radiation is broader along the y-axis for two colors [compare Fig. 3(c) and Fig. 3(e)]. Figure 3(d,f) show that the field values ~1 GV/m achieved inside the plasma are preserved at remote distances.

Leaking secondary fields. While the secondary transverse and longitudinal fields contain the THz signature of their respective nonlinear sources, it is not guaranteed that outside the plasma channel these components preserve their field strength - thus the transmitted THz power - all the way to the detector. Figure 4 answers this point by detailing the (y, z) maps of the electric field and x-magnetic components inside the plasma zone and transmitted in vacuum, once the pulse has propagated along the whole gas length ($t = 1200\,\omega_0^{-1}$). The free electron density (red color bar) and the field amplitude level (blue/green color bar) are specified. It is clearly seen that the THz field $\widetilde{E}_x$ created through photoionization keeps an amplitude ~GV/m comparable with the one produced inside the plasma tube, as already reported above. By contrast, $\widetilde{E}_y$ decreases by a factor ~2.5 and $\widetilde{E}_z$ vanishes rapidly. Along y, transverse ponderomotive forces generate obliquely-propagating THz pulses. This behavior can be understood from the ponderomotive source term $(\vec{J} \cdot \vec{\nabla})(\gamma \vec{J}/eN_e) \propto \partial_y E_L^2$ computed on the laser field Eq. (2), which is zero at $y = 0$ and maximum near $y = 10\,\mu$m. For comparison, the longitudinal field is maximum at center ($y = 0$), but its amplitude rapidly falls down outside the plasma channel. Amongst these two players, the transverse ponderomotive force hence conveys the highest THz field contribution, unlike the longitudinal field that becomes unable to transmit the THz pulse. As shown by Fig. 4(d), the peaks of the magnetic field $\widetilde{B}_x$ outside the plasma are mainly those of the $\widetilde{E}_y$ component. Inside the plasma region, $\widetilde{B}_x$ arises from the current components in the transverse gradients of the plasma profile. Spectrally, $\widetilde{B}_x$ keeps the signature of the transverse and longitudinal fields created inside the plasma channel, in such a way that it consists in the direct sum of $\widetilde{E}_y$ and $\widetilde{E}_z$ conical emissions. In this respect, Fig. 4(e–g) indeed display evidence that the longitudinal field spectrum $\widetilde{E}_z$ is non-zero at an angle larger than that of $\widetilde{E}_y$, so that $\widetilde{B}_x$ simply superimposes both contributions. In connection with Eq. (1),

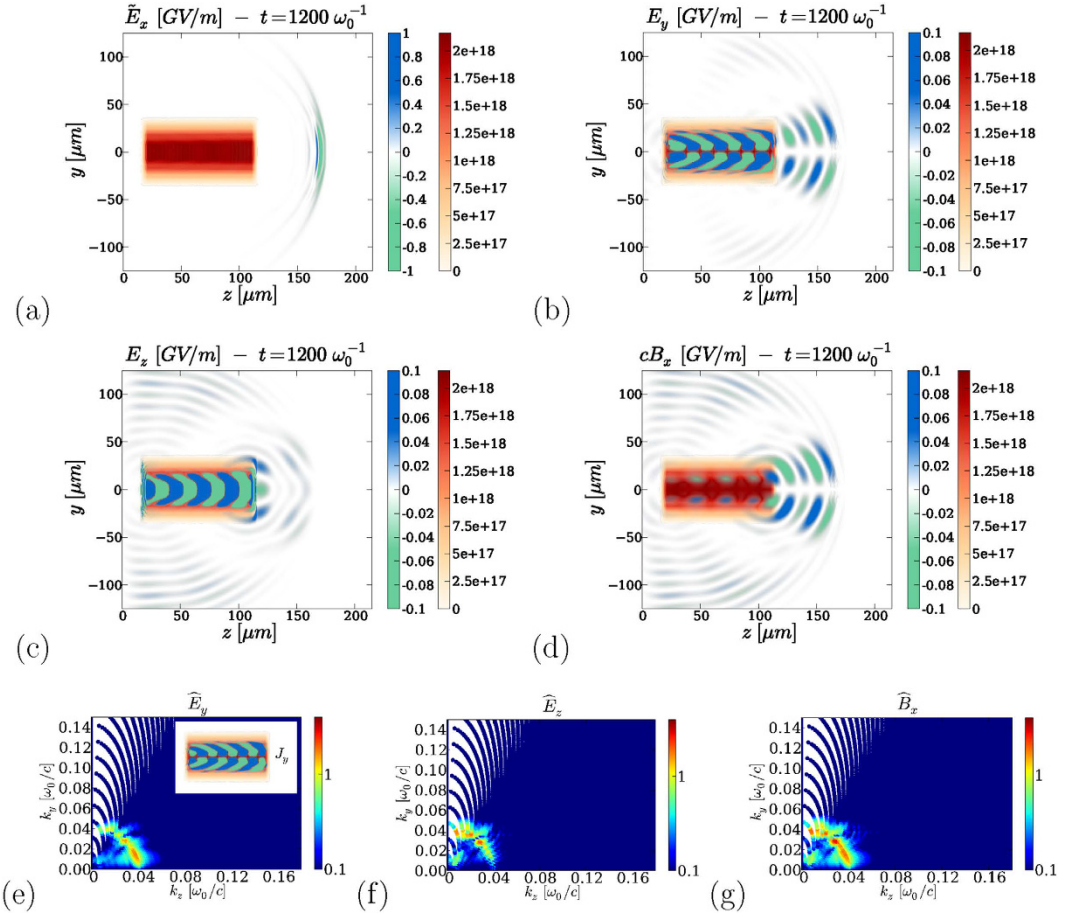

Figure 4. Two-color pulses for $I_0 = 5 \times 10^{16}$ W/cm^2. Top: (y, z) mapping of the fields emitted inside and outside the plasma channel at time t=1200 ω_0^{-1}. The left-hand side blue/green color bar indicates the field strength value in GV/m; the right-hand side red color bar indicates the electron density in cm^{-3}. (**a**) $\widetilde{E}_x$ (the laser field is filtered out), (**b**) E_y, (**c**) E_z and (**d**) cB_x. Bottom: Angular spectral distribution (arb. units) of (**e**) $\hat{E}_y$, (**f**) $\hat{E}_z$, and (**g**) $\hat{B}_x$ at $z = 175\,\mu$m. In (**e**) the inset represents the y-component of the current density generated inside the plasma.

the inset of Fig. 4(e) reveals that J_y is an odd function of y and has no on-axis spectral component [$\hat{J}_y(k_y = 0) = 0$]. The transverse ponderomotive currents, therefore, emit oblique THz waves, which was never reported before.

To end with, we present in Fig. 5(a) the energy converted to the THz and infrared domains over the 100-μm long plasma channel for the same laser characteristics as those of Fig. 4. We can see that the energy radiated outside the plasma region ($z = 175\,\mu$m) is located around the plasma frequency (~10 THz) due to wakefield and plasma wave emitters (B_x). Yet most of this energy results from photoionization (E_x) and accumulates over a broader frequency range. This property is reflected by the solid red line, plotting the cumulative distribution function in frequency (expressed in THz for better convenience). We moreover evaluated the optical energy lost through photoionization, backscattering and electron acceleration. These correspond to 0.06% of the input laser energy and amount to a conversion efficiency of about 2.6% over all the consumed laser energy in our frequency window. This value is weak, i.e., the plasma-to-THz conversion scheme is not optimal, but it is achieved over 100 μm of an underdense plasma only. For completeness, Fig. 5(b) details the evolution of the spatial structure of the laser field along the propagation range exceeding the plasma zone. This map clearly shows that over short propagation ranges the laser pulse profile remains preserved, which is consistent with the small energy losses.

The previous behaviors, of course, depend on the number of optical cycles contributing to THz pulse generation, on the initial gas atomic density and on the laser and plasma geometry. However, they should be generic. Figure 5(c,d) confirm this expectation by showing 2D PIC simulations of a two-color pulse whose fundamental has 17.5 fs FWHM duration and interacts with a twice higher initial density of atoms [Fig. 5(a)] or with a plasma profile having a longer gradient length [Fig. 5(b)]. The spectral pattern delivered by $\widetilde{E}_x$ exhibits a broader extent and higher amplitude, as fewer optical cycles render the pump profile more asymmetric[39], and there is a decrease in the ponderomotive spectral signal of $\widetilde{B}_x$ with longer density gradients[26]. Apart from these modifications, the THz spectra present generic features and we can anticipate that in a three-dimensional geometry the field distributions should remain close to the present ones, including solely an additional ponderomotive component along the x-axis.

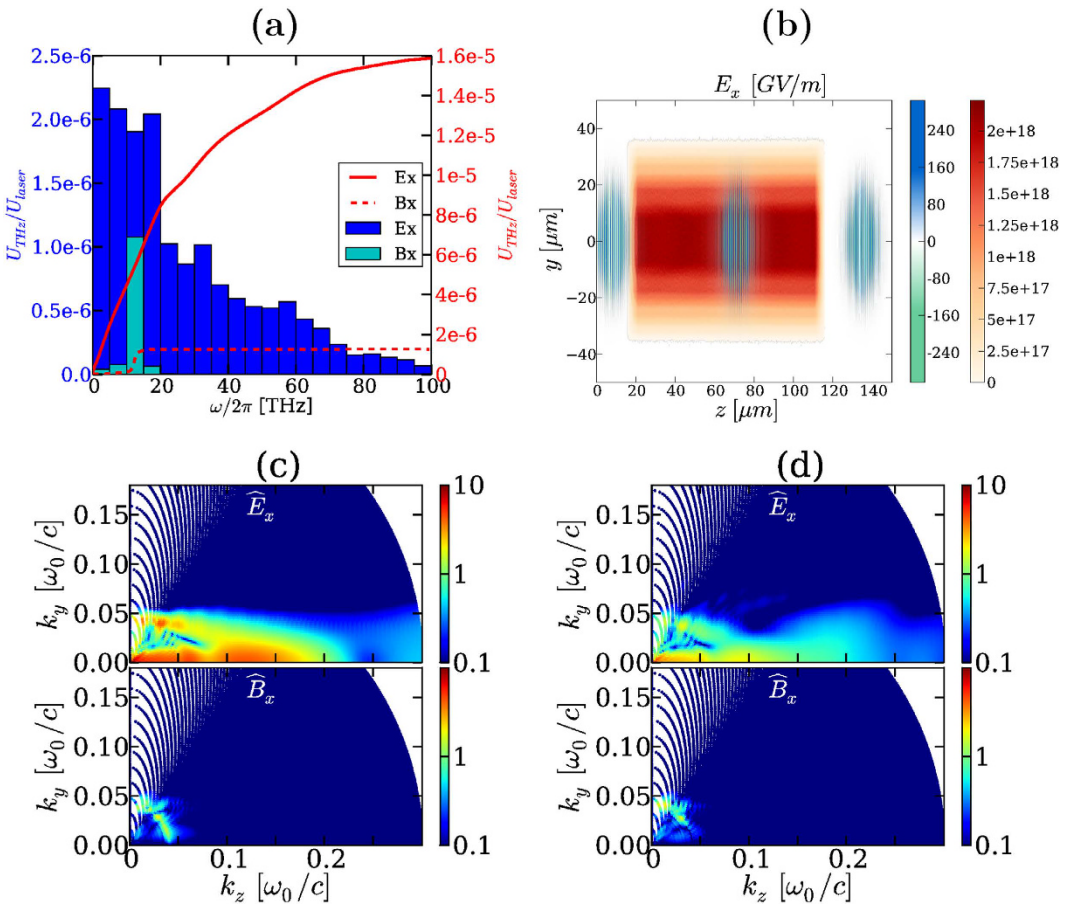

Figure 5. (**a**) THz energy distribution U_{THz} normalized to laser energy versus the electromagnetic frequency $\nu \equiv \omega/2\pi$ at $z = 175\,\mu$m in the two-color case with $I_0 = 5 \times 10^{16}\,\mathrm{W/cm^2}$ from the ponderomotive forces (B_x) and photocurrents (E_x). The solid line represents the cumulative distribution function in frequency that integrates the THz energy yields over the antecedent frequency domains. (**b**) Spatial map of the laser field E_x at three different propagation distances along and outside the plasma channel (the electron density is plotted in red). (**c,d**) Influence on the angular far-field spectra (arb. units) of the laser pulse duration and longitudinal plasma profile for the same intensity and (**c**) a pump FWHM of 17.5 fs (second harmonic length remains unchanged) and a higher initial ion density level $N_a \approx 5 \times 10^{17}\,\mathrm{cm^{-3}}$ at $z = 175\,\mu$m ($\varphi = 0$); (**d**) a longer plasma gradient [50 μm instead of 5 μm in the rear part of the plasma profile, which still extends over 100 μm; the laser parameters are unchanged compared with Fig. 1(c)]. The x-field spectrum radiated by photocurrents built from fewer optical cycles is broader and more intense.

Discussion

We reported PIC simulation results on the interaction of two-color laser Gaussian beams with an underdense plasma generating THz pulses. Our objective was to discriminate THz emissions promoted by photocurrents along the laser polarization axis from those produced by plasma wave oscillations that develop at high intensities. These results have been corroborated by a robust, semi-analytical 1D model. This model can be faithfully used for a broad range of laser intensities to predict THz fields occurring inside plasmas through photoionization and longitudinal wakefields in various experimental setups. We showed that, in the range of laser intensities between $10^{15}\,\mathrm{W/cm^2}$ and $3 \times 10^{17}\,\mathrm{W/cm^2}$ covering the domain of classical laser-driven plasma physics, THz pulse generation proceeds from both photoionization and ponderomotive forces. While the photocurrent mechanism prevails at intensities of $5 \times 10^{16}\,\mathrm{W/cm^2}$ in argon, the resulting THz field strength saturates when the relativistic limit $I_0 \to 10^{18}\,\mathrm{W/cm^2}$ is approached. This saturation stems from the fact that all outermost electrons of the valence shell have been ionized, leaving the ion in a relatively stable atomic state, unless resorting to much higher relativistic intensities. Finally, we demonstrated that the longitudinal fields alone rapidly decay away from the plasma and cannot transmit significant THz power remotely. It turns out that in multidimensional configurations the fields produced by transverse ponderomotive forces prevail outside the plasma zone over their longitudinal counterparts. Therefore, the radiated THz magnetic field along the laser polarization axis conveys the most relevant information on the plasma ponderomotive emitters.

Methods

2D PIC Simulations. Two-dimensional particle-in-cell simulations have been performed using the parallelized CALDER code[42], which solves the coupled set of Vlasov and Maxwell equations. This kinetic description, which entails a very large computational load, is required for the strongly nonequilibrium physics of intense laser-matter interaction. The Vlasov equation is solved by discretizing the plasma as a collection of charged "macro-particles". Maxwell equations are discretized on a regular, fixed and staggered Cartesian mesh according to the time-explicit Yee method. In our simulations, the resolution in space and time is $\Delta t = 0.079$ fs, $\Delta y = 0.48\,\mu$m, $\Delta z = 0.024\,\mu$m and the spectral step is $\Delta\nu = 0.47$ THz. The CALDER code includes Ammosov-Delone-Krainov (ADK)-based strong-field ionization modules[49] and Coulomb binary collisions[50]. Concerning the latter, we performed several tests on the impact of electron-electron and electron-ion collisions in the THz conversion efficiency and spectral patterns. We found a limited action of electron-electron collisions for intensities less than 10^{17} W/cm^2. Instead, electron-ion collisions dominate over long times and mainly condition the slow exponential damping of the longitudinal plasma waves. At larger, near-relativistic intensities, electron-electron collisions can, however, take over when the electrons acquire high drift velocities. For each simulation set, the collisional rate changes with the plasma characteristics and input laser parameters. Our code does not describe electron-neutral collisions, which is a valid approximation for sufficiently ionized plasmas. With free electron densities about $\approx 10^{18}$ cm^{-3} levels, electron-ion collisions always persist with an effective rate ν_c, which varies with the input laser intensity and the achieved electron density as ν_c [fs^{-1}] $\sim 7\times10^{-6} N_e$[cm^{-3}]$(W_{\rm osc}^2 + T_e^2)^{-3/2}$, where $W_{\rm osc} \sim I_0$ is the electron oscillation energy in the laser field and T_e denotes the electron temperature in eV[34]. Collisions thus decrease at increasing laser energy, up to the variations in the electron temperature that can reach ~0.1 keV in our intensity range. 2D PIC simulations indicate an effective electron-ion collision time of ~200 fs at 10^{15} W/cm^2 intensity, being characteristic of weakly ionized gases[13], of about 1 ps at 5×10^{16} W/cm^2 intensity, and a collision time larger than 10 ps at 3×10^{17} W/cm^2 intensity. All these values satisfy $\nu_c^2/4 \ll \tilde{\omega}_{\rm pe}^2$.

The next step consists in comparing 2D PIC simulations with a simpler 1D model discarding transverse ponderomotive and diffraction effects in the plasma. Semi-analytical solutions are then extracted from this 1D model, which enables us to approximate with accuracy the transverse and axial THz emissions for a broad intensity range.

Propagation equations. Working with high laser intensities and strong plasma excitations, we assume a minor role from bound electrons and discard all optical effects, such as Kerr self-focusing and chromatic dispersion. The laser pulse travels with group velocity equal to c and the plasma dynamics are described by the cold plasma fluid equation[28,51]

$$\partial_t \vec{p}_e + \nu_c \vec{p}_e + (\vec{v}_e\cdot\vec{\nabla})\vec{p}_e = -e\left(\vec{E} + \frac{\vec{p}_e}{m_e\gamma}\times\vec{B}\right) - \frac{\vec{p}_e}{N_e}S_{\rm ext}, \tag{12}$$

where $\vec{p}_e = \gamma m_e \vec{v}_e$ is the electron momentum [$\gamma = (1 - v_e^2/c^2)^{-1/2}$], $\vec{E}$ and $\vec{B}$ are the electric and magnetic fields, and N_e denotes the free electron density. $S_{\rm ext} \equiv \sum_{j=0}^{Z} j\partial_t N_j$ refers to the photoionization source where N_j are the ion densities evolving as

$$\frac{\partial N_j}{\partial t} = -W_{\rm ADK}^{j+1}N_j + W_{\rm ADK}^{j}N_{j-1},\ 0\le j\le Z, \tag{13}$$

where $\sum_j^Z N_j = N_a$, N_a and Z being the initial gas density and the atomic number, respectively[35]. The ADK-based ionization rate of complex atoms in the tunneling regime reads[47,49,52]

$$W_{\rm ADK}^{j}(E) = \frac{2^{\frac{8}{5}\left(n_j^*-1\right)}(2l_j+1)}{n_j^*\Gamma(2n_j^*)}\frac{\left\lfloor 4(U_i^j/U_H)^{\frac{5}{2}}\right\rfloor^{\frac{6n_j^*-1}{5}}\nu_a}{|E/E_a|^{2n_j^*-1}}e^{-\frac{2(U_i^j/U_H)^{\frac{3}{2}}}{3|E/E_a|}}, \tag{14}$$

where $n_j^* = j\sqrt{U_H/U_i^j}$ and l_j are the effective principal and orbital quantum numbers, U_i^j is the ionization energy of the jth electron of argon atoms[53], $\nu_a = 4.13\times10^{16}$ Hz, $E_a = 5.14\times10^{11}$ V/m (Hartree atomic units) and $U_H = 13.6$ eV is the ionization potential of hydrogen. The electron density N_e evolves as

$$\partial_t N_e - \frac{1}{e}\vec{\nabla}\cdot\vec{J} = S_{\rm ext}, \tag{15}$$

where the current density, neglecting ion motions, is given by $\vec{J} \simeq -eN_e\vec{v}_e$. Combining Eqs (12) and (15) straightforwardly yields Eqs (3) and (4). By using Maxwell equation $\vec{\nabla}\times\vec{B} = c^{-2}\partial_t\vec{E} + \mu_0\vec{J}$, these provide the propagation equation for $\vec{E}$:

$$\left(\partial_t^2 + c^2\vec{\nabla}\times\vec{\nabla}\times + \frac{\omega_{\rm pe}^2}{\gamma}\right)\vec{E} + (\partial_t\ \ln\ \gamma + \nu_c)(\partial_t\vec{E} + c^2\int_{-\infty}^{t}\vec{\nabla}\times\vec{\nabla}\times\vec{E}dt') = -\frac{\vec{\Pi}}{\varepsilon_0\gamma}, \tag{16}$$

where $\omega_{pe} = \sqrt{e^2 N_e/\varepsilon_0 m_e}$ is the standard electron plasma frequency. We here omit loss currents due to plasma absorption, which are small in underdense plasmas. The electric field $\vec{E}$ contains both the laser electric field polarized along the x-axis and the radiated field components.

Our one-dimensional model derives from Eq. (16). We neglect the diffraction operators ($\partial_x = \partial_y = 0$), yielding

$$(\partial_t \ln \gamma + \nu_c)(\partial_t^2 - c^2\partial_z^2)\int_{-\infty}^{t} E_x dt' + \left(\partial_t^2 - c^2\partial_z^2 + \frac{\omega_{pe}^2}{\gamma}\right)E_x = -\frac{\Pi_x}{\varepsilon_0\gamma}, \tag{17}$$

$$\left[\partial_t^2 + (\partial_t \ln \gamma + \nu_c)\partial_t + \frac{\omega_{pe}^2}{\gamma}\right]E_z = -\frac{\Pi_z}{\varepsilon_0\gamma}. \tag{18}$$

Next we evaluate the source terms $\vec{\Pi}$ of Eq. (4) on the laser field and thus need to determine the associated current density. Its expression proceeds from equation (3), for which an underlying hypothesis is always $v_e^2 \ll c^2$ for massive (electron) particles. In these conditions, the ponderomotive terms such as $(\vec{J}\cdot\vec{\nabla})(\gamma\vec{J}/eN_e)$ can be assumed of second order, so that

$$(\partial_t + \nu_c)\gamma J_x = \frac{e^2 N_e}{m_e}E_x + \frac{e}{m_e}J_z B_y, \tag{19}$$

$$(\partial_t + \nu_c)\gamma J_z = \frac{e^2 N_e}{m_e}E_z - \frac{e}{m_e}J_x B_y, \tag{20}$$

where $B_y = -\partial_z\int_{-\infty}^{t} E_x dt'$. E_z is the longitudinal field produced by the laser field and obeying Gauss law

$$\vec{\nabla}\cdot\vec{E} = \partial_z E_z = \frac{e}{\varepsilon_0}\left(\sum_{j=0}^{Z} jN_j - N_e\right). \tag{21}$$

Further approximations are requested to achieve a tractable theoretical model. First, we limit our intensity range to marginally-relativistic intensities, i.e., the normalized laser vector potential satisfies $a_L \leq 0.5$, corresponding to laser intensities $I_0 \leq 3\times 10^{17}\,\mathrm{W/cm^2}$. This amounts to considering relativistic factors $\gamma \simeq (1 + a_L^2)^{1/2} \leq 1.12$. So, γ is valued to only about 10% above unity and we assume it constant ($\partial_t\gamma \simeq 0$). Second, the last term of Eq. (4) vanishes when it is computed in the laser region, since the photoionization model supposes $\partial_t N_e = S_{ext}$ for electrons ionized with zero velocity at the electric field maxima[36]. Because $\partial_x J_x = 0$, transverse ponderomotive effects are ignored and thus

$$\Pi_x = \frac{e}{m_e}J_z B_y,\ \Pi_z = -\frac{e}{m_e}J_x B_y. \tag{22}$$

By virtue of Eq. (15), since J_z is initiated by the laser field, function of $(z - ct)$, the electron density $N_e(t)$ expresses as

$$N_e(t) = -\frac{J_z(t)}{ec} + \sum_{j=0}^{Z} jN_j(t). \tag{23}$$

The transverse field. To find out the transverse field, we transform Eq. (17) by applying $\partial_t \ln\gamma = 0$ together with Eq. (22) and $B_y = -\partial_z\int_{-\infty}^{t} E_x dt' = E_x/c$ for B_y travelling like the laser pulse, from which

$$(\partial_t^2 - c^2\partial_z^2)(\partial_t + \nu_c)E_x = -\partial_t(\widetilde{\omega}_{pe}^2 E_x) \tag{24}$$

easily follows and is further numerically solved. Using $J_x = \varepsilon_0(\partial_t + \nu_c)^{-1}\widetilde{\omega}_{pe}^2 E_x$ and splitting $J_x = J_L + \tilde{J}_x$ on the expansion $E_x = E_L + \widetilde{E}_x$, the previous equation produces Eq. (6).

We re-express this equation in the variables $\tau = t - z/c$, $\eta = ct$. By assuming a constant effective plasma frequency $\widetilde{\omega}_{pe}$ in its left-hand side and ignoring the η-derivatives in the weak collisional term $\approx(1 + \nu_c/\partial_\tau)^{-1}$, a direct Fourier transform gives the spectrum of $\widetilde{E}_x$, Eq. (11), where

$$g(z,\omega) = -\frac{1}{\delta\varepsilon_0\widetilde{\omega}_{pe}^2}\left[1 + e^{iz\omega/c}\left\{\frac{i\omega}{\sqrt{\omega^2 + \delta\widetilde{\omega}_{pe}^2}}\sin\left(\frac{z}{c}\sqrt{\omega^2 + \delta\widetilde{\omega}_{pe}^2}\right) - \cos\left(\frac{z}{c}\sqrt{\omega^2 + \delta\widetilde{\omega}_{pe}^2}\right)\right\}\right],$$
$$\delta \equiv \frac{1}{1 + i\nu_c/\omega}, \tag{25}$$

involves the propagation variable z for which the pulse center is $\tau = 0$ in the group-velocity frame. $\widetilde{E}_x$ can then be extracted by inverse Fourier transform.

Alternatively, solutions to Eq. (24) can be sought as $E_x(t, z) = E_L(z - ct) + \widetilde{E}_x$ inside two distinct domains[39]: the so-called "beam head" domain, in which the radiated field $\widetilde{E}_x$ is small in front of the laser field, $\widetilde{E}_x \ll E_L$ for $\tau < \tau_p$. In that case the right-hand side of Eq. (24) reduces to $-\partial_t(\widetilde{\omega}_{pe}^2 E_L)$. By solving the resulting equation in the co-moving frame travelling with the laser pulse group velocity $\tau = t - z/c$ and $\xi = z$ along the characteristics $(\tau - \tau_0)/2 = (\xi_0 - \xi)/c$, one extracts Eq. (9).

Behind the beam head, for long times $\tau \gg \tau_p$, $\widetilde{E}_x$ is computed from $(\partial_t^2 - c^2\partial_z^2 + \widetilde{\omega}_{pe}^2)\widetilde{E}_x = 0$ in the limit of weak collisions. By means of Laplace transforms, the solution $\widetilde{E}_x$ consists of residual plasma oscillations shaped by the Bessel function of the first kind, which forces the field to decay like $\sim 1/\sqrt{t}$ over long times (see Debayle *et al.*[39] for technical details).

The longitudinal field. Since E_x is dominated by the laser field E_L, B_y reduces to $B_L = E_L/c$ in Π_x, $J_x \approx J_L$ and the longitudinal radiated field $\widetilde{E}_z$ obeys

$$(\partial_t^2 + \nu_c\partial_t + \widetilde{\omega}_{pe}^2)\widetilde{E}_z = \frac{e}{m_e\varepsilon_0\gamma c}J_L E_L \equiv D_z(t), \tag{26}$$

which is nothing else but Eq. (7). Here we approximate N_e by the sum $\sum_{j=0}^{Z} jN_j$ at first order, i.e., the effective plasma frequency $\widetilde{\omega}_{pe}^2$ is not an implicit function of $\widetilde{E}_z$ and it is defined by Eq. (8). Equation (26) has thus the direct solution:

$$\widetilde{E}_z(t) = \int_{-\infty}^{t} \frac{e^{-\nu_c(t-t')/2}}{\sqrt{\widetilde{\omega}_{pe}^2(t') - \nu_c^2/4}} \sin\left[\int_{t'}^{t} \sqrt{\widetilde{\omega}_{pe}^2(t'') - \nu_c^2/4}\, dt''\right] D_z(t')dt'. \tag{27}$$

When the right-hand side term of Eq. (18) is evaluated through the slowly-varying envelope function (5), the corresponding magnetic field and current density admit the following decompositions:

$$\overrightarrow{B}_L = \frac{1}{2}(\mathcal{B}_{\omega_0}e^{i\psi_{\omega_0}} + \mathcal{B}_{2\omega_0}e^{i\psi_{2\omega_0}} + c.c.)\overrightarrow{e}_y,\ \overrightarrow{J}_L = \frac{1}{2}(\mathcal{J}_{\omega_0}e^{i\psi_{\omega_0}} + \mathcal{J}_{2\omega_0}e^{i\psi_{2\omega_0}} + c.c.)\overrightarrow{e}_x, \tag{28}$$

where, for $\Omega_0 = \omega_0$ or $2\omega_0$,

$$\mathcal{B}_{\Omega_0} = \frac{1}{c}\left(1 + \frac{i\partial_t}{\Omega_0}\right)^{-1}\left(1 - \frac{ic\partial_z}{\Omega_0}\right)\mathcal{E}_{\Omega_0},\ \mathcal{J}_{\Omega_0} = \frac{e^2}{\gamma m_e(\nu_c - i\Omega_0)}\left(1 + \frac{\partial_t}{\nu_c - i\Omega_0}\right)^{-1} N_e\mathcal{E}_{\Omega_0}. \tag{29}$$

Applying the slowly-varying envelope approximation $\partial_t \ll \Omega_0$, we readily find

$$D_z(t) \simeq \frac{e\widetilde{\omega}_{pe}^2}{4\gamma m_e c}\sum_{\Omega_0=\omega_0,2\omega_0}\left[2\nu_c + 2\frac{(\Omega_0^2 - \nu_c^2)}{\Omega_0^2 + \nu_c^2}\frac{\partial_t N_e}{N_e} - c\partial_z\right]\frac{\left|E_{\Omega_0}\right|^2}{\nu_c^2 + \Omega_0^2}, \tag{30}$$

and Eq. (27) reproduces Eq. (10) using $\nu_c \ll \widetilde{\omega}_{pe}$, Ω_0 and $-c\partial_z\mathcal{E}_{\Omega_0} = \partial_t\mathcal{E}_{\Omega_0}$. Similar expressions were earlier derived by Sprangle *et al.* and D'Amico *et al.* for a single wave ($\Omega_0 = \omega_0$) in the non-relativistic limit $\gamma = 1$[28,37]. Besides $\gamma \neq 1$, the three differences with these former works are the following.

1. In Eqs (26) and (27), the product of the rapid variations of $N_e(t)$ in $\widetilde{\omega}_{pe}^2$ through photoionization in the beam head $[\partial_t N_e(t) \sim S_{ext}]$ yields non-zero field contributions in the THz domain.
2. We account for wakefield plasma oscillations linked to a non-zero longitudinal field ($J_z \neq 0$) increasing from high enough laser intensities.
3. Our model equations apply to two-color pulses and can easily be extended to more colors.

The characteristic behaviors of the emitted fields and additional validations of Eqs (6) and (7) compared to solutions of Eqs (17) and (18) are detailed in the Supplementary Information. They confirm that the one-dimensional model provides us with a good tool for interpreting 2D PIC simulations of laser-driven THz radiations in the plasma region.

References

1. Tonouchi, M. Cutting-edge terahertz technology. *Nature Photon.* **1,** 97 (2007).
2. Thomson, M. D., Kress, M., Löffler, T. & Roskos, H. G. Broadband THz emission from gas plasmas induced by femtosecond optical pulses: From fundamentals to applications. *Laser Photon.& Rev.* **1,** 349 (2007).
3. Tuniz, A. *et al.* Metamaterial fibres for subdiffraction imaging and focusing at terahertz frequencies over optically long distance. *Nature Commun.* **4,** 2706 (2013).
4. Xie, X., Dai, J. & Zhang, X. C. Coherent control of THz wave generation in ambient air. *Phys. Rev. Lett.* **96,** 075005 (2006).
5. Liu, J., Dai, J., Chin, S. L. & Zhang, X.-C. Broadband terahertz wave remote sensing using coherent manipulation of fluorescence from asymmetrically ionized gases. *Nature Photon.* **4,** 627 (2010).
6. Chan, W. L., Deibel, J. & Mittleman, D. M. Imaging with terahertz radiation. *Rep. Prog. Phys.* **70,** 1325 (2007).
7. Yeh, K.-L., Hoffmann, M. C., Hebling, J. & Nelson, K. A. Generation of 10 μJ ultrashort THz pulses by optical rectification. *Appl. Phys. Lett.* **90,** 171121 (2007).
8. Stepanov, A. G., Bonacina, L., Chekalin, S. V. & Wolf, J.-P. Generation of 30 μJ single-cycle terahertz pulses at 100 Hz repetition rate by optical rectification. *Opt. Lett.* **33,** 2497 (2008).
9. Stepanov, A. G. *et al.* Mobile source of high-energy single-cycle terahertz pulses. *Appl. Phys. B: Lasers & Optics* **101,** 11 (2010).

10. Vicario, C., Monoszlai, B. & Hauri, C. P. GV/m single-cycle terahertz fields from a laser-driven large-size partitioned organic crystal. *Phys. Rev. Lett.* **112,** 213901 (2014).
11. Cook, D. J. & Hochstrasser, R. M. Intense terahertz pulses by four-wave rectification in air. *Opt. Lett.* **25,** 1210 (2000).
12. Kim, K. Y., Taylor, A. J., Glownia, J. H. & Rodriguez, G. Coherent control of terahertz supercontinuum generation in ultrafast laser-gas interactions. *Nature Photon*. **2,** 605 (2008).
13. Babushkin, I. *et al.* Ultrafast spatiotemporal dynamics of terahertz generation by ionizing two-color femtosecond pulses in gases. *Phys. Rev. Lett.* **105,** 053903 (2010).
14. Chin, S. L. *et al.* The propagation of powerful femtosecond laser pulses in optical media: Physics, applications, and new challenges. *Can. J. Phys.* **83,** 863 (2005).
15. D'Amico, C. *et al.* Conical forward THz emission from femtoseond-laser-beam filamentation in air. *Phys. Rev. Lett.* **98,** 235002 (2007).
16. Wang, T. J. *et al.* High energy terahertz emission from two-color laser-induced filamentation in air with pump pulse duration control. *Appl. Phys. Lett.* **95,** 131108 (2009).
17. Daigle, J. F. *et al.* Remote THz generation from two-color filamentation: long distance dependence. *Opt. Express* **20,** 6825 (2012).
18. Kosareva, O. G. *et al.* Analysis of dual frequency interaction in the filament with the purpose of efficiency control of THz pulse generation. *J. Infrared Milli. Terahz. Waves* **32,** 1157 (2011).
19. Bergé, L., Skupin, S., Köhler, C., Babushkin, I. & Herrmann, J. 3D numerical simulations of THz generation by two-color laser filaments. *Phys. Rev. Lett.* **110,** 073901 (2013).
20. Oh, T. I. *et al.* Intense terahertz generation in two-color laser filamentation: energy scaling with terawatt laser systems. *New J. Phys.* **15,** 075002 (2013).
21. You, Y. S., Oh, T. I. & Kim, K. Y. Off-axis phase-matched terahertz emission from two-color laser-induced plasma filaments. *Phys. Rev. Lett.* **109,** 183902 (2012).
22. Magesh Kumar, K. K., Kumar, M., Yuan, T., Sheng, Z. M. & Chen, M. Terahertz radiation from plasma filament generated by two-color laser gas-plasma interaction. *Laser & Part. Beams* **33,** 473 (2015).
23. Matsubara, E., Nagai, M. & Ashida, M. Ultrabroadband coherent electric field from far infrared to 200 THz using air plasma induced by 10 fs pulses. *Appl. Phys. Lett.* **101,** 011105 (2012).
24. Gopal, A. *et al.* Observation of gigawatt-class THz pulses from a compact laser-driven particle accelerator. *Phys. Rev. Lett.* **111,** 074802 (2013).
25. Gopal, A. *et al.* Observation of energetic terahertz pulses from relativistic solid density plasmas. *New J. Phys.* **14,** 083012 (2012).
26. Liao, G. Q. *et al.* Bursts of terahertz radiation from large-scale plasmas irradiated by relativistic picosecond laser pulses. *Phys. Rev. Lett.* **114,** 255001 (2015).
27. Wang, W.-M. *et al.* Efficient terahertz emission by mid-infrared laser pulses from gas targets. *Opt. Lett.* **36,** 2608 (2011).
28. Sprangle, P., Peñano, J. R., Hafizi, B. & Kapetanakos, C. A. Ultrashort laser pulses and electromagnetic pulse generation in air and on dielectric surfaces. *Phys. Rev. E* **69,** 066415 (2004).
29. Gildenburg, V. B. & Vvedenskii, N. V. Optical-to-THz wave conversion via excitation of plasma oscillations in the tunneling-ionization process. *Phys. Rev. Lett.* **98,** 245002 (2007).
30. Buccheri, F. & Zhang, X.-C. Terahertz emission from laser-induced micro plasma in ambient air. *Optica* **2,** 366 (2015).
31. Singh, M. & Sharma, R. P. Generation of THz radiation by laser plasma interaction. *Contrib. Plasma Phys.* **53,** 540 (2013).
32. Wang, W. M. *et al.* Strong terahertz pulse generation by chirped laser pulses in tenuous gases. *Opt. Express* **16,** 16999 (2008).
33. Balakin, A. V., Borodin, A. V., Kotelnikov, I. A. & Shkurinov, A. P. Terahertz emission from a femtosecond laser focus in a two-color scheme. *J. Opt. Soc. Am. B* **27,** 16 (2010).
34. Peñano, J., Sprangle, P., Hafizi, B., Gordon, D. & Serafim, P. Terahertz generation in plasmas using two-color laser pulses. *Phys. Rev. E* **81,** 026407 (2010).
35. Debayle, A., González de Alaiza Martínez, P., Gremillet, L. & Bergé, L. Non-monotonic increase in laser-driven THz emissions through multiple ionization events. *Phys. Rev. A* **91,** 041801 (2015).
36. Babushkin, I. *et al.* Tailoring terahertz radiation by controling tunnel photoionization events in gases. *New J. Phys.* **13,** 123029 (2011).
37. D'Amico, C. *et al.* Forward THz radiation emission by femtosecond filamentation in gases: theory and experiment. *New J. Phys.* **10,** 013015 (2008).
38. Chen, M., Pukhov, A., Peng, X.-Y. & Willi, O. Theoretical analysis and simulations of strong terahertz radiation from the interaction of ultrashort laser pulses with gases. *Phys. Rev. E* **78,** 046406 (2008).
39. Debayle, A., Gremillet, L., Bergé, L. & Köhler, C. Analytical model for THz emissions induced by laser-gas interaction. *Opt. Express* **22,** 13691 (2014).
40. Clerici, M. *et al.* Wavelength scaling of terahertz generation by gas ionization. *Phys. Rev. Lett.* **110,** 253901 (2013).
41. Panov, N. *et al.* Directionality of terahertz radiation emitted from an array of femtosecond filaments in gases. *Laser Phys. Lett.* **11,** 125401 (2014).
42. Lefebvre, E. *et al.* Electron and photon production from relativistic laser plasma interactions. *Nucl. Fusion* **43,** 629 (2003).
43. Li, M. *et al.* Verification of the physical mechanism of THz generation by dual-color ultrashort laser pulses. *Appl. Phys. Lett.* **101,** 161104 (2012).
44. Schmid, K. *et al.* Density-transition based electron injector for laser driven wakefield accelerators. *Phys. Rev. ST Accel. Beams* **13,** 091301 (2010).
45. Kaganovitch, D., Gordon, D. F., Helle, M. H. & Ting, A. Shaping gas jet plasma density profile by laser generated shock waves. *J. Appl. Phys.* **116,** 013304 (2014).
46. Andreeva, V. A. *et al.* Ultrabroad terahertz spectrum generation from an air-based filament plasma. *Phys. Rev. Lett.* **116,** 063902 (2016).
47. González de Alaiza Martínez, P. & Bergé, L. Influence of multiple ionization in laser filamentation. *J. Phys. B: At. Mol. Opt. Phys.* **47,** 204017 (2014).
48. González de Alaiza Martínez, P. *et al.* Boosting terahertz generation in laser-field ionized gases using a sawtooth wave shape. *Phys. Rev. Lett.* **114,** 183901 (2015).
49. Nuter, R. *et al.* Field ionization model implemented in particle in cell code and applied to laser-accelerated carbon ions. *Phys. Plasmas* **18,** 033107 (2011).
50. Pérez, F., Gremillet, L., Decoster, A., Drouin, M. & Lefebvre, E. Improved relativistic collisions and collisional ionization in PIC codes. *Phys. Plasmas* **19,** 083104 (2012).
51. Shadwick, B. A., Schroeder, C. B. & Esarey, E. Nonlinear laser energy depletion in laser-plasma accelerators. *Phys. Plasmas* **16,** 056704 (2009).
52. Ammosov, M. V., Delone, N. B. & Kraĭnov, V. P. Tunnel ionization of complex atoms and of atomic ions in an alternating electromagnetic field. *Sov. Phys. JETP* **64,** 1191 (1986).
53. *NIST Atomic Spectra Database.*

Acknowledgements
L.B. thanks Stefan Skupin and Illia Thiele for discussions on modelling aspects. X.D. thanks Mathieu Lobet for help on vizualisation tools. All authors acknowledge PRACE for awarding us access to the supercomputer CURIE at GENCI@CEA, France.

Author Contributions
P.G.d.A.M. conceived the Maxwell-Fluid model, performed 1D simulations and worked on the analytical model together with A.D. X.D. performed the 2D PIC simulations, L.G. analysed the results and L.B. derived the model. All authors reviewed the manuscript.

Additional Information
Supplementary information accompanies this paper at http://www.nature.com/srep

Competing financial interests: The authors declare no competing financial interests.

How to cite this article: González de Alaiza Martínez, P. *et al.* Terahertz radiation driven by two-color laser pulses at near-relativistic intensities: Competition between photoionization and wakefield effects. *Sci. Rep.* **6**, 26743; doi: 10.1038/srep26743 (2016).

SCIENTIFIC REPORTS

OPEN

Corrigendum: Terahertz radiation driven by two-color laser pulses at near-relativistic intensities: Competition between photoionization and wakefield effects

P. González de Alaiza Martínez, X. Davoine, A. Debayle, L. Gremillet & L. Bergé

Scientific Reports **6**:26743; doi: 10.1038/srep26743; published online 03 June 2016; updated on 28 September 2016

This Article contains a typographical error in Equation 1,

$$\frac{d^2\mathcal{E}}{d\omega d\Omega} = \frac{cr^2}{\pi\mu_0}|\vec{\nabla}\times\widehat{\vec{A}}(\omega,\vec{r})|^2 = \frac{\omega^2L^2}{16\varepsilon_0\pi^3c^3}\mathrm{sinc}^2\left[\frac{\omega L}{c}(1-\cos\theta)\right]|\vec{n}\times\widehat{\vec{J}}(\omega,\vec{k}_\perp)|^2.$$

should read:

$$\frac{d^2\mathcal{E}}{d\omega d\Omega} = \frac{cr^2}{\pi\mu_0}|\vec{\nabla}\times\widehat{\vec{A}}(\omega,\vec{r})||^2 = \frac{\omega^2L^2}{16\varepsilon_0\pi^3c^3}\mathrm{sinc}^2\left[\frac{\omega L}{2c}(1-\cos\theta)\right]|\vec{n}\times\widehat{\vec{J}}(\omega,\vec{k}_\perp)|^2.$$